Origin of the Selective Electroreduction of Carbon Dioxide to Formate by Chalcogen Modified Copper

- Supporting Information -

Origin of the Selective Electroreduction of Carbon Dioxide to Formate by Chalcogen Modified Copper

Rodrigo García-Muelas,[1] Federico Dattila,[1] Tatsuya Shinagawa,[2] Antonio J. Martín,[2] Javier Pérez-Ramírez,[2] and Núria López[1]**

[1]Institute of Chemical Research of Catalonia. The Barcelona Institute of Science and Technology. Av. Països Catalans 16, 43007 Tarragona, Spain

[2]Institute for Chemical and Bioengineering, Department of Chemistry and Applied Biosciences, ETH Zürich. Vladimir-Prelog-Weg 1, 8093 Zurich, Switzerland

Corresponding Author

*jpr@chem.ethz.ch (J.P.-R), *nlopez@iciq.es (N.L.)

TABLE OF CONTENTS:

1. Experimental Procedures

Chalcogen modified copper materials were synthesized via a solvothermal route.[1,2] In a typical preparation, copper nitrate ($Cu(NO_3)_2 \cdot 3H_2O$; Sigma-Aldrich, 99.0%, 4 mmol) and elemental chalcogen (sulfur (Sigma-Aldrich, > 95%, 0.067 mmol), selenium (Alfa Aesar, 99.999%, 0.2 mmol, or tellurium (Fluka, ≥ 99.999%, 0.2 mmol)) were mixed in ethylene glycol (Sigma-Aldrich, 99%, 40 cm^3) at room temperature for > 30 min. The mixture was transferred into a 50-cm^3 Teflon-lined autoclave, heated (413 K, 12 h) and then allowed to naturally cool to room temperature. The resulting solid was washed with ultrapure water (18.2 MΩ cm) three times by centrifugation (6000 rpm, 10 min) and the obtained powders were dried under vacuum overnight at 353 K. In the same manner, an unmodified Cu_2O catalyst (Cu-∅) was prepared without addition of elemental chalcogen.

The catalysts were deposited on carbon gas diffusion layers (GDL; Sigracet 39BC, SGL Group) by airbrushing. An ink was prepared by dispersing 50 mg of the powder in the mixed solution of ultrapure water (4 cm^3) and 2-propanol (Sigma-Aldrich, 99.8%, 4 cm^3), into which 5 wt% Nafion solution (Sigma-Aldrich, 50 mm^3) was added as a binder phase. The resulting slurry was sonicated for 15 min, and then sprayed onto the GDL with an airbrush (Iwata Eclipse HP-SBS) at 353 K. A catalyst loading of 1-2 mg cm^{-2} was typically achieved.

The electrochemical CO_2 reduction reaction (eCO_2RR) was investigated for 1.5 h by chronoamperometry (CA). A custom gas-tight glass cell with two chambers separated by a Nafion 212 membrane (Alfa Aesar, 0.05 mm thickness) was employed to this end. Both catholyte and anolyte chambers were filled with 40 cm^3 of a 0.1 M $KHCO_3$ solution (Sigma-Aldrich, 99.95% trace metals basis). Before and during the measurement, CO_2 (Messer, purity 4.8) was fed to the catholyte at a flow rate of 20 cm^3 min^{-1}. A Pt wire and a Ag/AgCl (3.0 M

KCl) were used as counter and reference electrodes, respectively. The geometric surface area of the cathodes (around 2 cm^2) was accurately quantified with the ImageJ image processing and analysis software (Wayne Rasband, National Institutes of Health). All measurements were performed employing an Autolab PGSTAT302N potentiostat at room temperature. The double layer capacitance was assessed by cyclic voltammetry (CV), which was conducted at varying scan speeds in the potential range of open circuit potential ±15 mV. CAs were performed with the *iR* compensation function set at 85% of the uncompensated resistance (R_u), which was determined before the start of the CAs and updated every 10 min by electrochemical impedance spectroscopy at the electrolysis potential (10 kHz, 10 mV amplitude). The remaining 15% was corrected manually by the R_u. The potentials reported herein are referenced to the reversible hydrogen electrode (RHE). Current densities were normalized by the geometric surface area.

Gaseous products were analyzed using an on-line gas chromatograph (GC; SRI 8610C, Multi-Gas #3 configuration) with Ar as a carrier gas equipped with a HayeSep D column and a Molecular Sieve 13X column. Samples were injected through a sampling loop and analyzed 10 min after the start of the electrolysis and thereafter every 20 min. The Faradaic efficiencies ($\eta_{i,g}$) for gas products were calculated from Equation S1.

$$\eta_{i,g} = \frac{vC_i n_e F}{j} 100\% \quad \text{(Equation S1)}$$

where v is the volumetric flow of gas, C_i is the concentration of product i, j is the electric current at sampling time, n_e is the number of electrons transferred, and F is the Faraday constant. Liquid products were analyzed with a high-performance liquid chromatograph in a Merck LaChrom system equipped with a Bio-Rad Aminex HPX-87H column heated at 333 K and a refractive index detector (Hitachi Chromaster 5450) using 5 mM H_2SO_4 as eluent, or with a nuclear magnetic resonance (NMR; Bruker UltraShield 300MHz). The Faradaic efficiencies for the

liquid products ($\eta_{i,l}$) were quantified by analyzing the catholyte after the eCO_2RR test using Equation S2, where V is the catholyte volume and Q the total charge passed during the electrolysis.

$$\eta_{i,l} = \frac{VC_i n_e F}{Q} 100\% \quad \text{(Equation S2)}$$

X-ray diffraction (XRD) patterns were acquired with a PANalytical X'Pert PRO-MPD diffractometer with Bragg-Brentano geometry using Ni-filtered Cu Kα radiation (λ = 0.1541 nm). The patterns were recorded in the 10-70° 2θ range with an angular step size of 0.05° and a counting time of 180 s per step. X-ray photoelectron spectroscopy (XPS) analysis was carried out with a PHI Quantum 2000 spectrometer (Physical Electronics) equipped with a 180° spherical capacitor energy analyzer, at a base pressure of 5×10^{-7} Pa using monochromatic Al Kα radiation (1486.68 eV). The binding energy scale was calibrated with the C 1s signal at 284.8 eV. Values of sulfur at.% include removal of the Nafion binder contribution upon estimation based on the quantification of the F content, solely ascribable to the binder. Scanning electron microscopy (SEM) and back-scattered electron micrographs and Energy-dispersive X-ray (EDX) spectroscopy maps (5 kV acceleration voltage) were acquired in a FEI Quanta 200F instrument. Powdered samples were dispersed in dry form onto fresh carbon paint deposited on an aluminum holder. Time of flight secondary ion mass spectroscopy (ToF-SIMS) was applied by using an IONTOF TOF.SIMS 5 instrument. During analysis, a Bi^{1+} primary ion beam (25 keV), in combination with an electron flood gun for charge compensation, was scanned over an area of 250 × 250 μm^2 with a 0.5 pA target current for 80 s. The resulting primary ion dose density (PIDD) is 2.45×10^8 cm^{-2} and well below static SIMS limit. Spectra of positively and negatively charged secondary ions were acquired on fresh surface regions. Due to sample topography the resulting mass resolution was limited to a range between R = 4000 to 6000.

2. Computational Details

The Density Functional Theory (DFT) calculations were done in VASP.[3,4] We chose the PBE density functional[5] including dispersion through the DFT-D2 method,[6,7] with the reparametrization of C_6 coefficients for metals performed by our group.[8] Implicit solvation was included within the VASP-MGCM framework, but were not included when computing activation energies.[9,10] Inner electrons were represented by PAW pseudopotentials[11,12] and the monoelectronic states for the valence electrons expanded as plane waves with a kinetic energy cutoff of 450 eV. The catalyst was modeled considering four metal surfaces, Cu(111), (211), (110) and (100). They contained at least four layers, where the two uppermost were fully relaxed and the rest fixed to the bulk distances. In the systems containing a chalcogen (*X* = O, S, Se, Te), the coverage ranged between 1/9 and 1/16 ML. The Brillouin zone was sampled by a Γ-centered k-points mesh from the Monkhorst-Pack method,[13] with a reciprocal grid size smaller than 0.03 $Å^{-1}$. The vacuum between the slabs was larger than 12 Å. The adsorbates were placed only on one side of the slab, thus requiring a dipole correction to remove spurious contributions arising from the asymmetric slab model.[14] The structures of $*CO_2^-$ and XCO_2^- were obtained from single-point calculations by removing a hydrogen from $*CO_2H$ and XCO_2H. All energies are reported using as references: CO_2(g), H_2(g), and the Cu surface, either clean or chalcogen-doped. The relative energy between the H^+ and the H_2(g) at U = 0.0 V was obtained from the computational hydrogen electrode.[15,16] Conversely, the energies of HCO_2^- and HX^- were obtained from their corresponding conjugated acids from Equation S3.

$$G_{B^-} = G_{HB} - k_B T \ln(10)(\mathrm{pH} - \mathrm{pKa}) \quad \text{(Equation S3)}$$

3. Cation Effect

The herein developed model describing the eCO_2RR over the chalcogen modified copper surfaces points to the significance of charged intermediates species. Their presence suggests a considerable impact of the identity of the alkali metal cation present in the electrolyte on the energy levels of the intermediate. With this in mind, we carried out electrolyses over the Cu-S, which exhibited the highest activity and selectivity toward formate (Figure 1c), in CO_2-saturated carbonate electrolytes with various cations (Li^+, Na^+, K^+, or Cs^+). Our experimental results (Figure S8a) indeed demonstrated that the identity of the alkali metal cation substantially modifies the catalytic response. Notably, cations with larger atomic number simultaneously favored the eCO_2RR and inhibited the formation of H_2, as reflected in the partial current densities (Figure S8a), while keeping the exclusive formation of formate among carbon products. We note that this behavior is consistent with recent studies[17–19] relating larger cations to increased mitigation of local pH alteration due to the induced local hydrolysis[18] and the stabilization of surface intermediates via electrostatic interactions with the solvated cation.[19] Our model quantitatively rationalizes the role and function of the alkali metal cation during the eCO_2RR. Our calculations support the electrostatic effects as in ref 17 and 19 as the responsible for the increased activity and selectivity as one of the key intermediates is stabilized by the electrostatic interactions with CO_2^- species. To interact with the intermediate, the cation needs to be partially desolvated (1/3 of its first coordination sphere), and thus the lower the solvation energy, the larger the overall energy for the intermediate stabilization. In Figure S8b, the experimentally observed partial current densities for hydrogen and formate are plotted as a function of the solvation energy of the cations. The coordination of these cations with the solvent should move from six to four to efficiently interact with the formate.

4. Supplementary Schemes and Figures

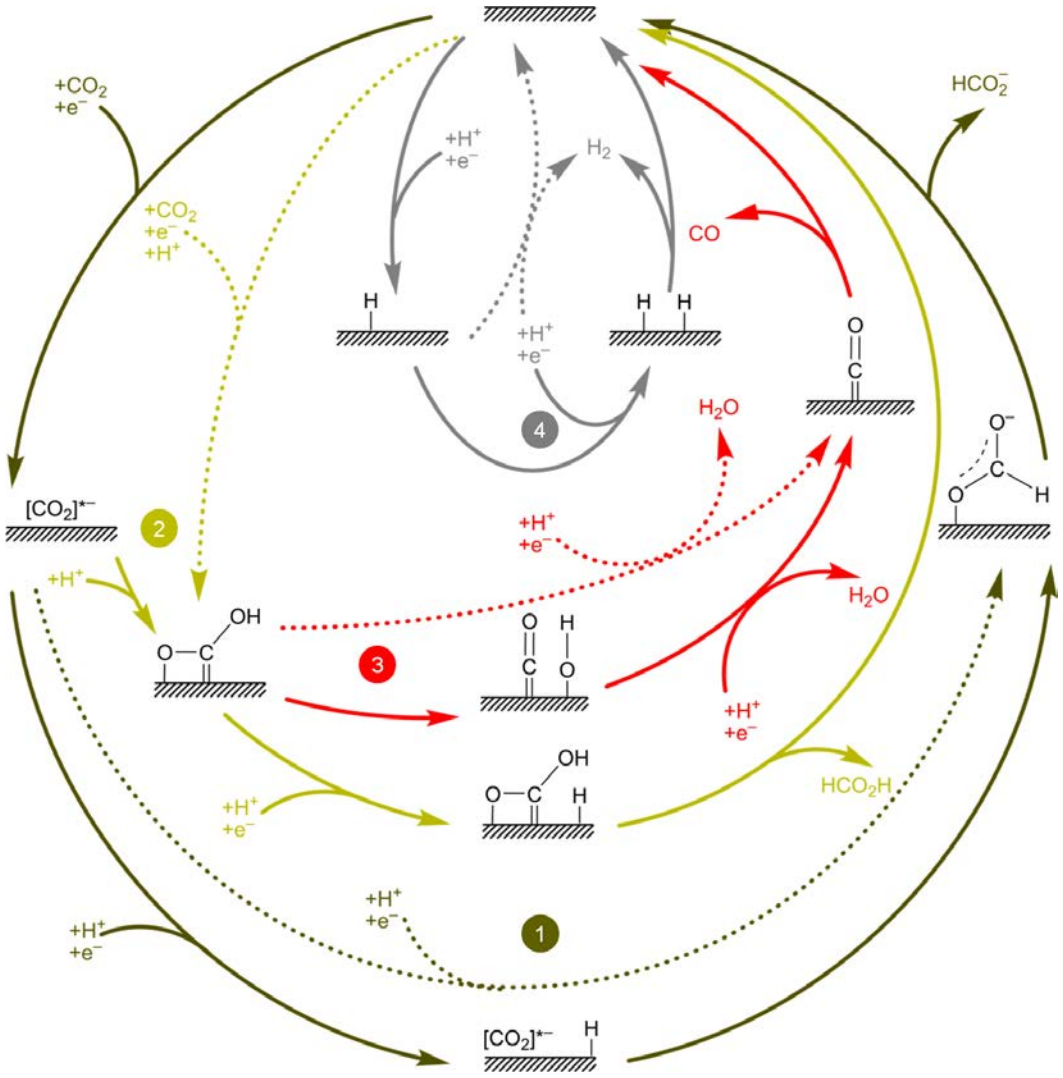

Scheme S1. Reaction Mechanism for the Electrochemical Reduction of CO_2 on Clean Cu Surfaces. The Reaction Paths toward Formate Is Shown in Dark and Light Yellow. Upon Desorption, the Formic Acid Produced on Path 2 Converts to Formate on Neutral and Basic pH. The Parasitic Reaction Paths toward CO and H_2 Is Shown in Red and Gray Respectively. Adsorbed Carbon Dioxide Is Shown as $[CO_2]^{*-}$ Since It Has Different Conformations Under Working Potentials, Figure S15a. Several PCET Shortcuts That Cannot Be Discarded Are Shown as Dotted Lines.

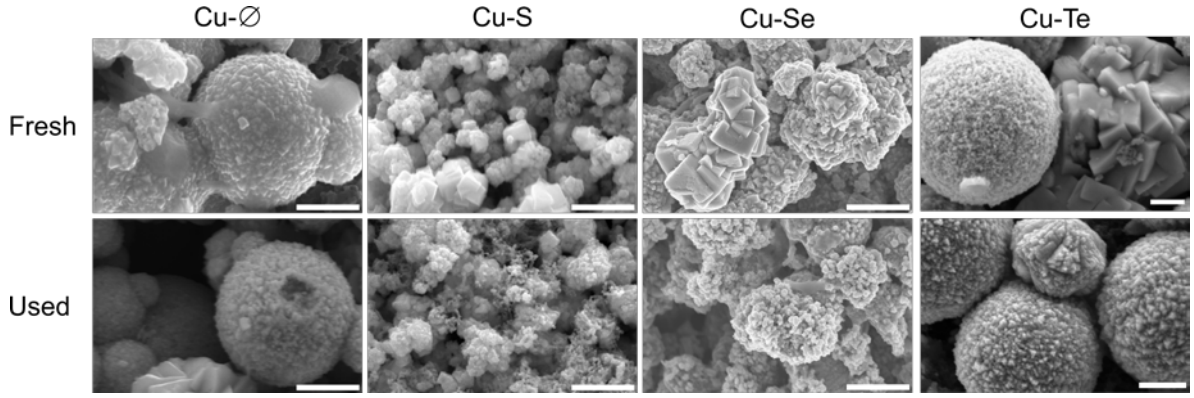

Figure S1. SEM images of the submicron-sized particles of copper-chalcogen catalysts before and after the eCO_2RR testing at −0.6 V vs RHE. Scale bars: 1 μm.

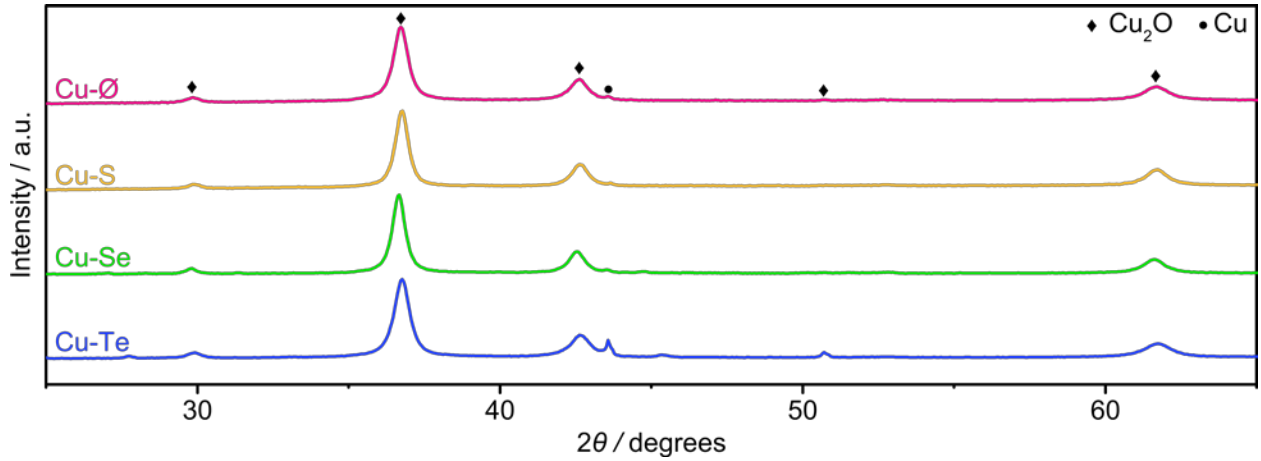

Figure S2. XRD diffractograms of the fresh copper-chalcogen catalyst powders. The average crystalline sizes estimated by using the Scherrer equation based on the diffraction peak at the (111) facet were 11.0, 11.2, 11.4, and 11.5 nm for Cu-Ø, Cu-S, Cu-Se, and Cu-Te, respectively.

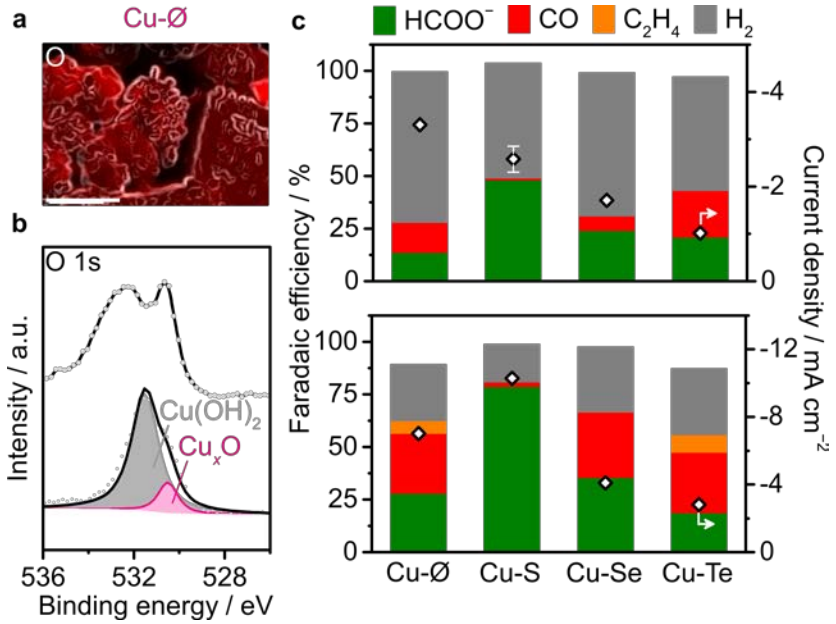

Figure S3. (a) EDX elemental maps of oxygen for the Cu-Ø catalyst. White contours indicating the particle borders are added as a visual aid (see Figure S4). Scale bar: 2 μm. (b) XPS spectra in the O 1s region of the Cu-Ø before and after the eCO_2RR testing at −0.6 V vs RHE. (c) Product distribution over copper-chalcogen catalysts, obtained by chronoamperometry at −0.6 (top) and −0.8 V (bottom) vs RHE for 1.5 h in 0.1 M $KHCO_3$ saturated with CO_2 (pH 6.7). Adopted from Figure 1 in the main text.

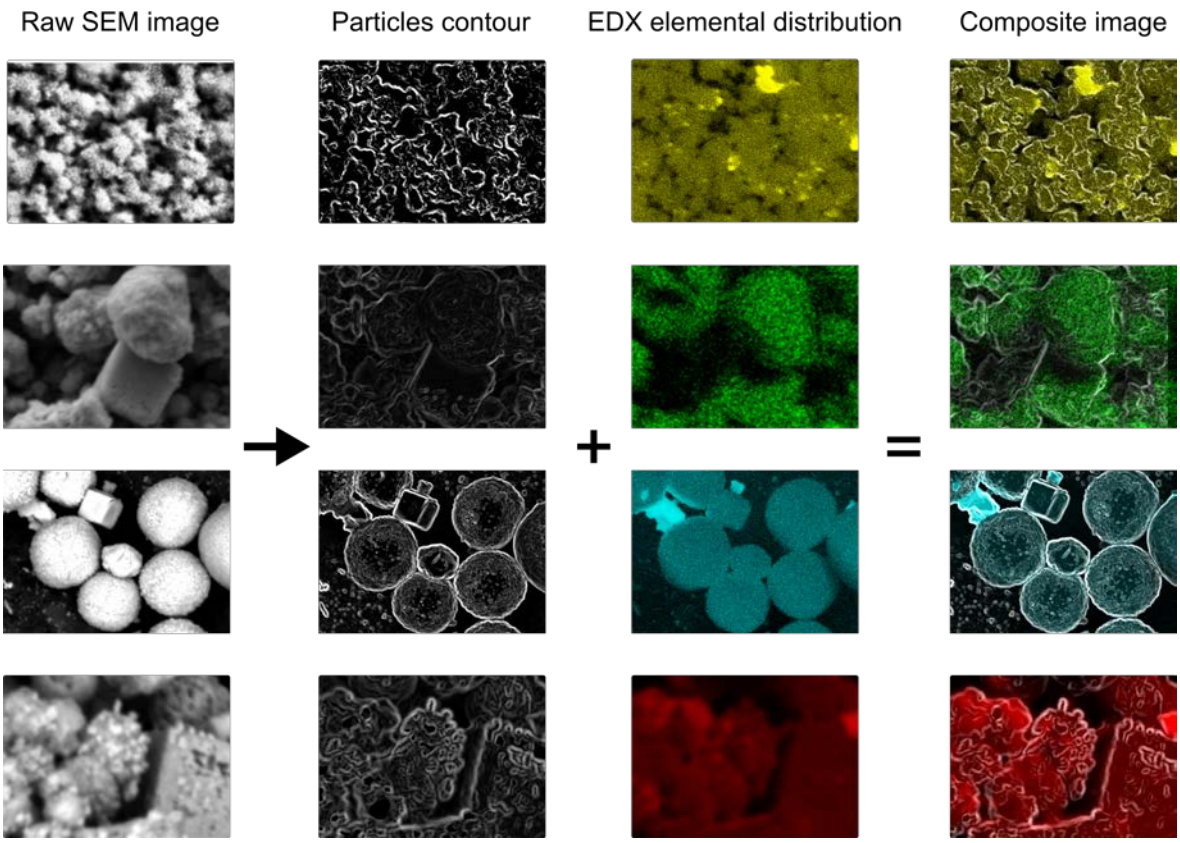

Figure S4. Contours of particles were extracted by processing SEM micrographs and overlaid with elemental maps to create composite maps showing elemental distribution. Cu-S, Cu-Se, Cu-Te and Cu-Ø systems shown respectively from top to bottom.

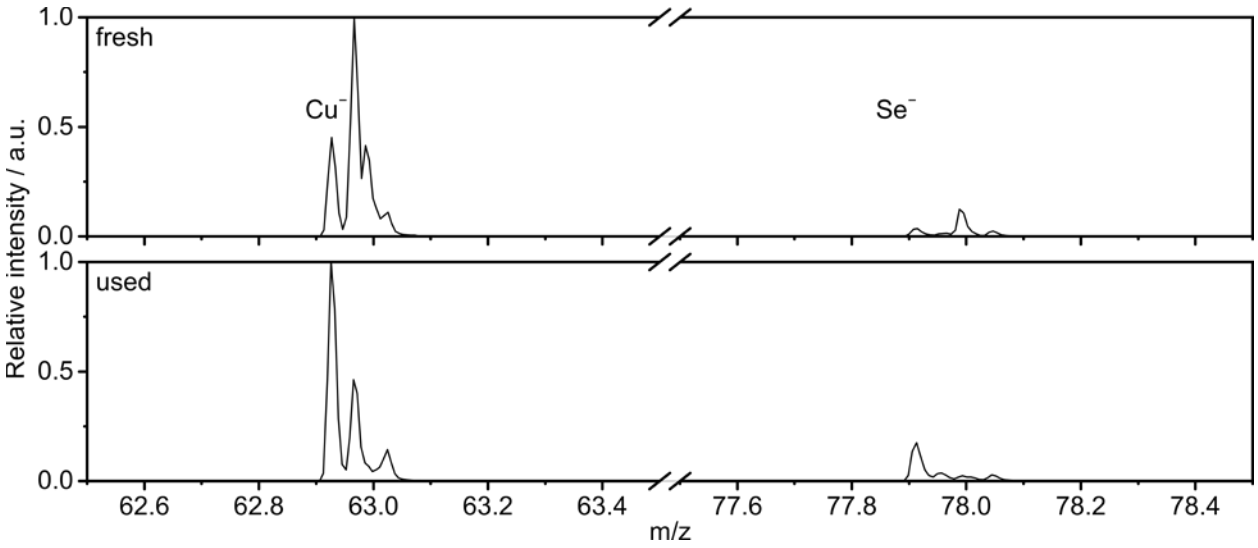

Figure S5. ToF-SIMS spectra of the Cu-Se catalyst before and after the eCO_2RR testing at −0.6 V vs RHE. The signal intensity originating from Se^- (m/z = 77.9) relative to Cu^- (m/z = 62.9) was determined to be 9% in the fresh catalyst and 18% for the spent catalyst.

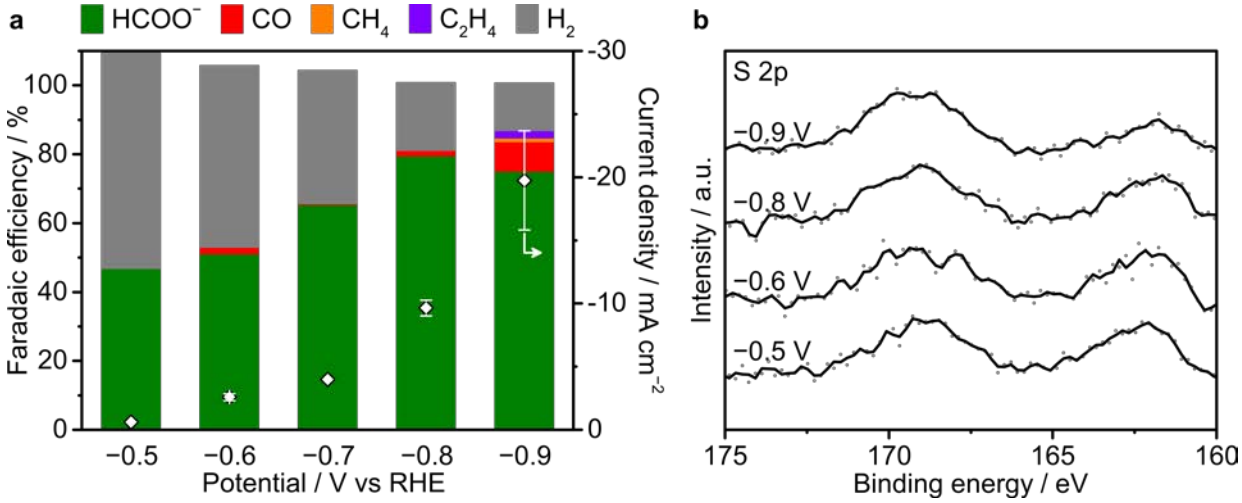

Figure S6. (a) Activity of the Cu-S catalysts as a function of the electric potential, obtained by CA for 1.5 h in 0.1 M $KHCO_3$ saturated with CO_2 (pH 6.7). (b) XPS spectra in the S 2p region of Cu-S catalysts after the eCO_2RR testing at denoted potentials. The peak associated to sulfide phases at ca. 162 eV decreased upon exposure to –0.9 V vs RHE, suggesting leaching of the sulfur modifier, in line with the incipient selectivity change observed at that potential. Data are adopted from our previous study.[1]

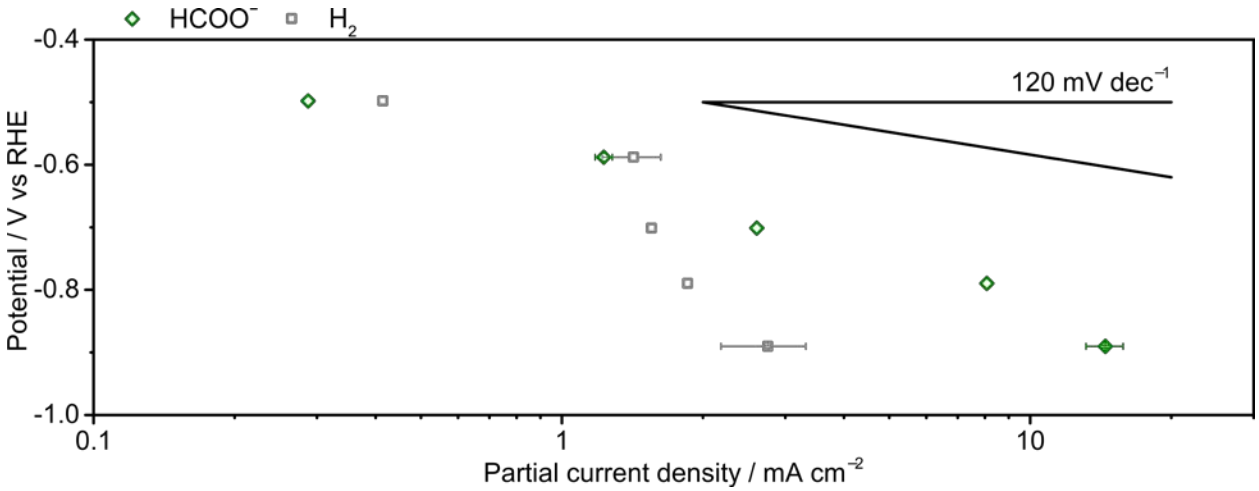

Figure S7. Experimental Tafel plot for formate production and hydrogen evolution reaction over the Cu-S. Data obtained by CA for 1.5 h in 0.1 M $KHCO_3$ saturated with CO_2 (pH 6.7).

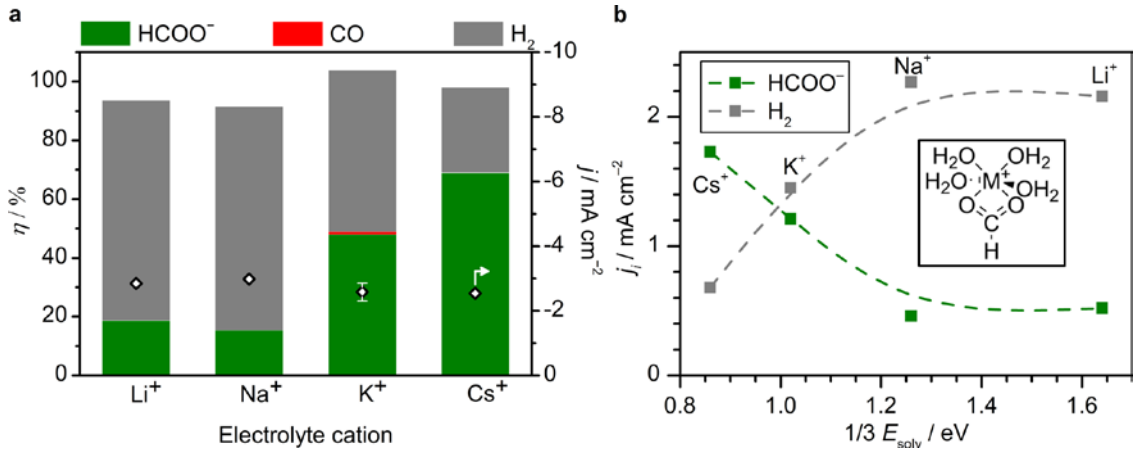

Figure S8. Effect of alkali cations on the performance of sulfur-modified copper catalyst. (a) product distribution over sulfur-modified copper obtained by CA at −0.6 V vs RHE for 1.5 h in carbonate solution with various cations (Li^+, Na^+, K^+ or Cs^+) saturated with CO_2 (pH 6.7) at room temperature. (b) Partial current density as a function of the Gibbs free energy of solvation for the cations. Dashed lines serve as guides to the eye. Inset: The solvated alkali cations, coordinated to six water molecules, can stabilize HCO_2^- only after de-coordinating two water molecules in their first solvation shell. This accounts for roughly 1/3 of the total solvation energy.

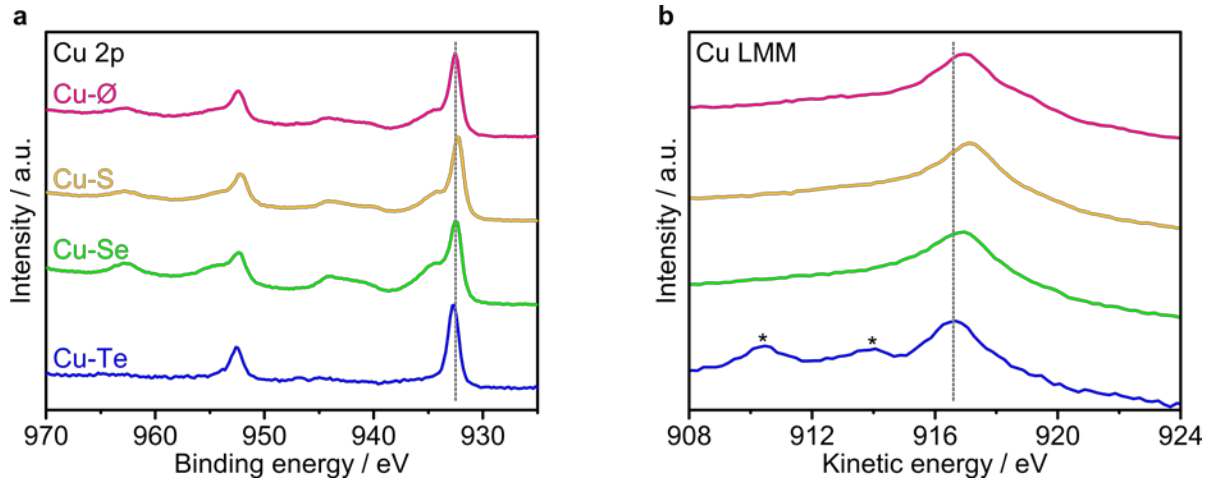

Figure S9. (a) XPS analysis in the Cu 2p region of the copper-chalcogen catalysts. (b) Auger emission spectroscopy (AES) analysis in the Cu LMM region of the copper-chalcogen catalysts. The vertical lines are added as a visual aid, highlighting the large similarity among materials. The peaks indicated by asterisk (*) originate from the excitation in the Te 3d orbital. The excitation around the Cu 2p region shown in (a) exhibited a sharp peak at around 933 eV for all copper-chalcogen catalysts ascribable to Cu_2O ($2p_{3/2}$), while a broad peak (approximately 936 eV) accompanied by the broad satellite in the range of 940~945 eV indicated the presence of Cu^{2+}. Further information arose from the AES spectra in the Cu LMM region shown in (b), displaying a signal centered at 917 eV ascribable to Cu_2O, consistent with the Cu 2p spectra.[20]

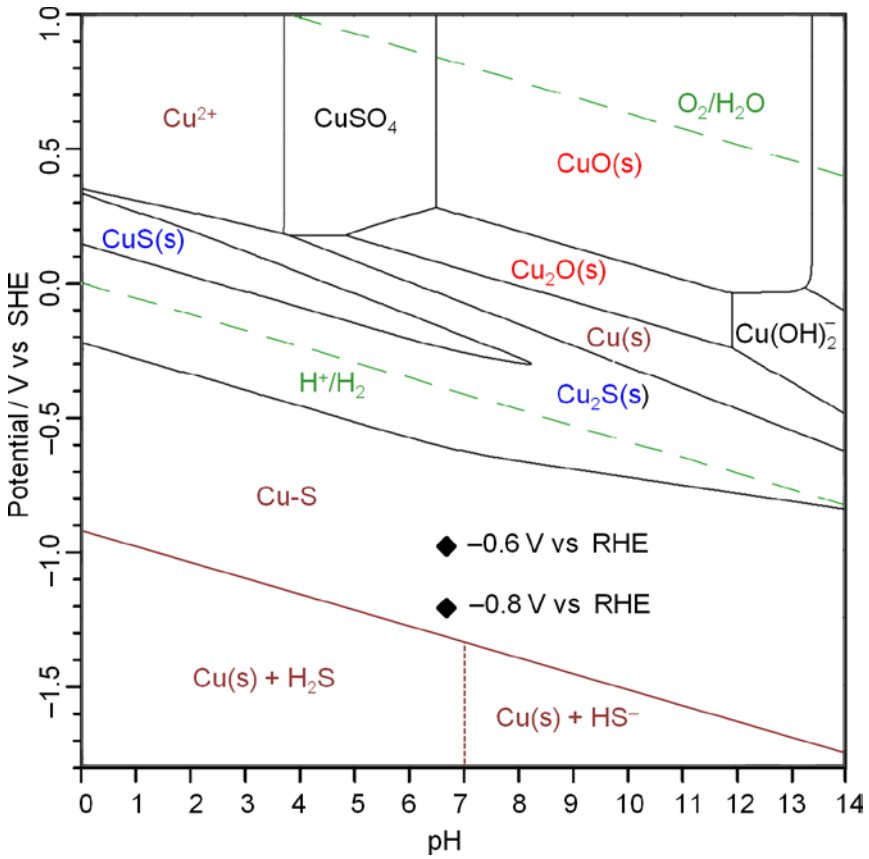

Figure S10. Pourbaix diagram for the Cu-O-S system generated using the *HydraMedusa* package.[21] The equilibrium lines are calculated at 298 K, [HS^-] = 5 mM, and [Cu^{2+}] = 10.00 µM. The plot is in good agreement with analogous reported in ref 22 and 23. The dark red line has been added derived from the present DFT data on Cu-S stability (Table S2). Therefore, the S adatom-modified Cu system is the stable phase at working potentials (black diamonds).

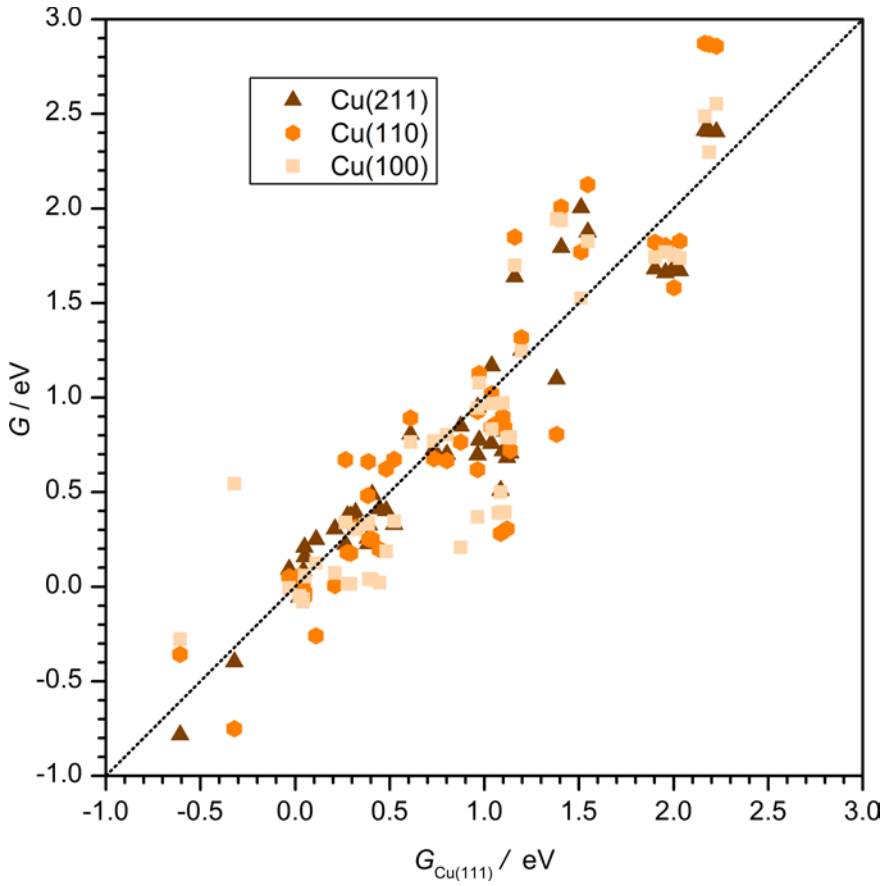

Figure S11. Gibbs free energies of intermediates on Cu(211), (110), and (100) are closely correlated to the free energies on Cu(111), whether or not coadsorbed chalcogen atoms are present. Thus, the analysis of the energy profiles of all the facets yield qualitatively the same results.

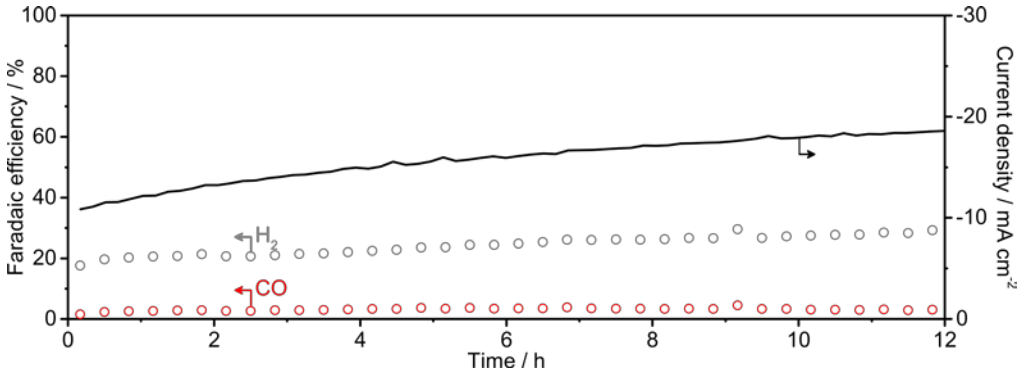

Figure S12. Faradaic efficiency to gaseous products (red and gray circles toward CO and H_2 respectively) and total current density (black line) obtained at −0.8 V vs RHE over a 12 h CA using the Cu-S catalyst. Average Faradaic efficiency to formate was 73%, determined by a High-Performance Liquid Chromatography. Data are adopted from our previous study.[1]

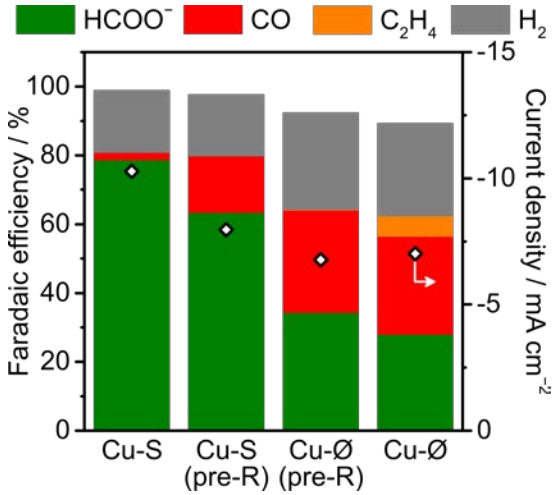

Figure S13. Product distribution obtained by CA at −0.8 V vs RHE for 1.5 h over the Cu-S, a pre-reduced Cu-S, a pre-reduced Cu-Ø, and the Cu-Ø. The pre-reduction was carried out by CA at −1.1 V vs RHE for 1.5 h. Cu-S and Cu-Ø values are reproduced from Figure 1 in the main text. The selectivity pattern of the pre-reduced Cu-S drifted toward that of the corresponding unmodified material, suggesting the partial loss of sulfur from the surface. Electrolyte: 0.1 M $KHCO_3$ saturated with CO_2 (pH 6.7).

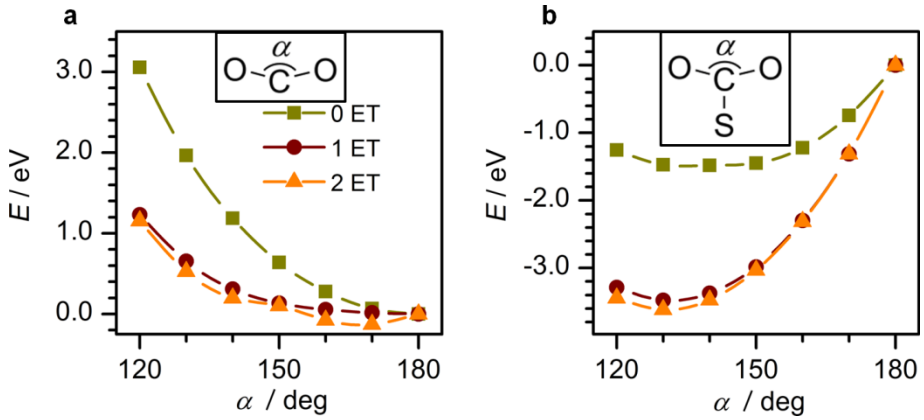

Figure S14. Potential energy of (a) CO_2 and (b) thiocarbonate (SCO_2) as a function of the activation angle, α, defined in the inset. Dark red and orange lines include the values when 1 or 2 electrons have been transferred to the system, respectively. Thus, CO_2 activation is promoted by electron transfers (ET) and basic centers, $X^{\delta-}$.

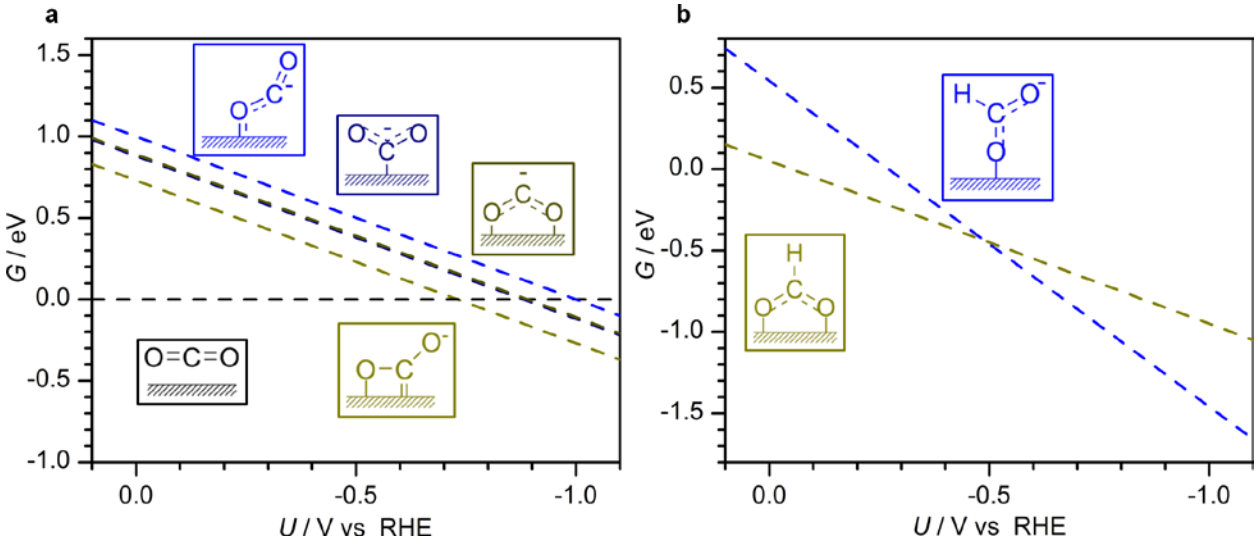

Figure S15. Relative stability of the conformation of (a) CO_2 and (b) formate adsorbed on Cu(111). For U = 0.0 V vs RHE, the chemisorption of CO_2 is endergonic by +0.73 to +1.00 eV, depending on the conformation. Bader analysis reveals that these species take charge from the surface. The non-bounded state is shown in black. The electron transfer from the Cu surface stabilizes the chemisorbed intermediates at potentials deeper than –0.73 eV vs RHE, starting by the η^2(C,O) conformation (light yellow) followed by η^1(C) and η^2(O,O), which are degenerated. Similarly, for formate, at U = 0.0 V vs RHE, the potential energy of the monodentate conformation (HCOO*$^-$, blue) is 0.75 eV higher than the bidentate (HCOO**, dark yellow), so the former one has been chosen on previous theoretical studies. The implicit solvent reduces this difference by stabilizing the monodentate form more than the bidentate (–0.40 vs –0.14 eV). When Gibbs free energies are computed including electron transfers, the monodentate conformation becomes more stable for potentials lower than –0.49 V vs RHE, close to the working potentials employed in this study.

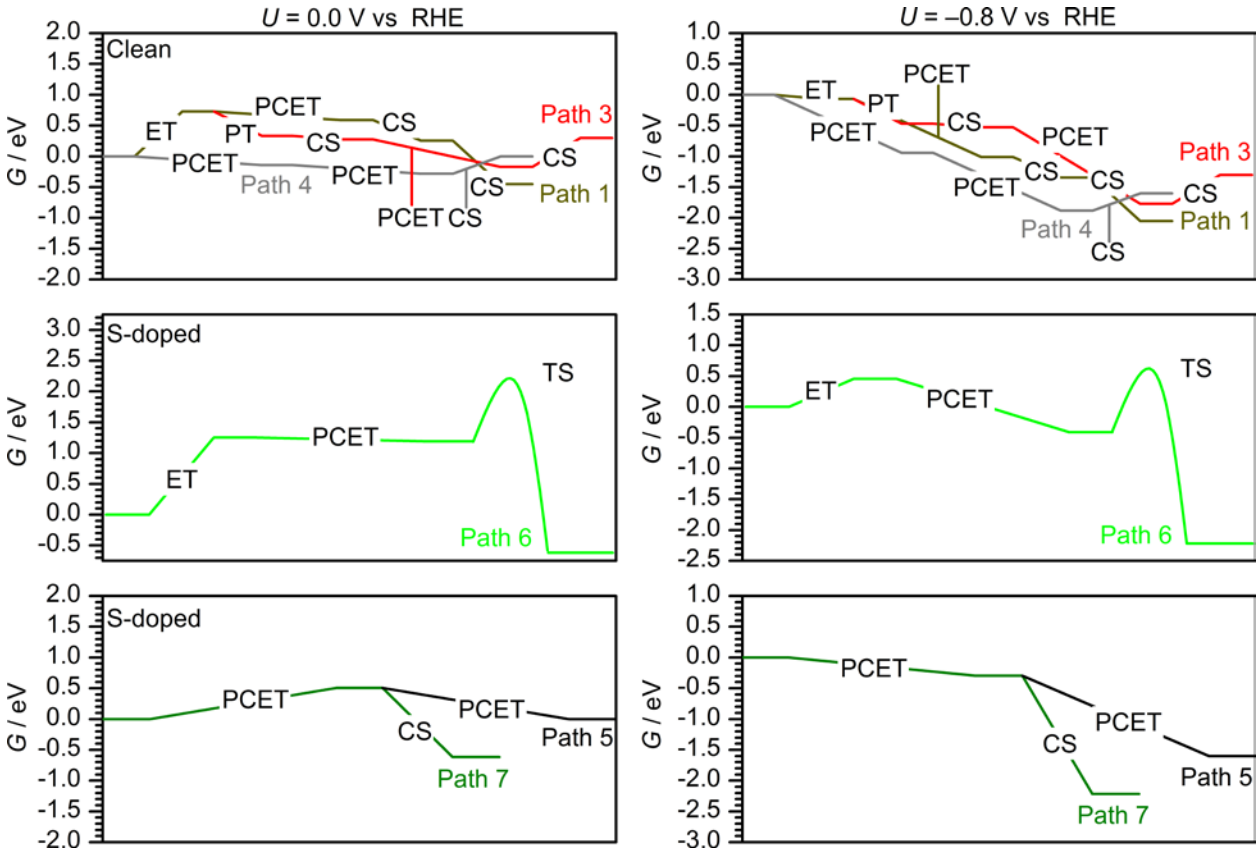

Figure S16. Reaction profiles for CO_2 reduction and hydrogen evolution reactions on clean and chalcogen modified Cu(111) surfaces at U = 0.0 and –0.8 V vs RHE. The colors of the reaction paths are selected according to Scheme 1.

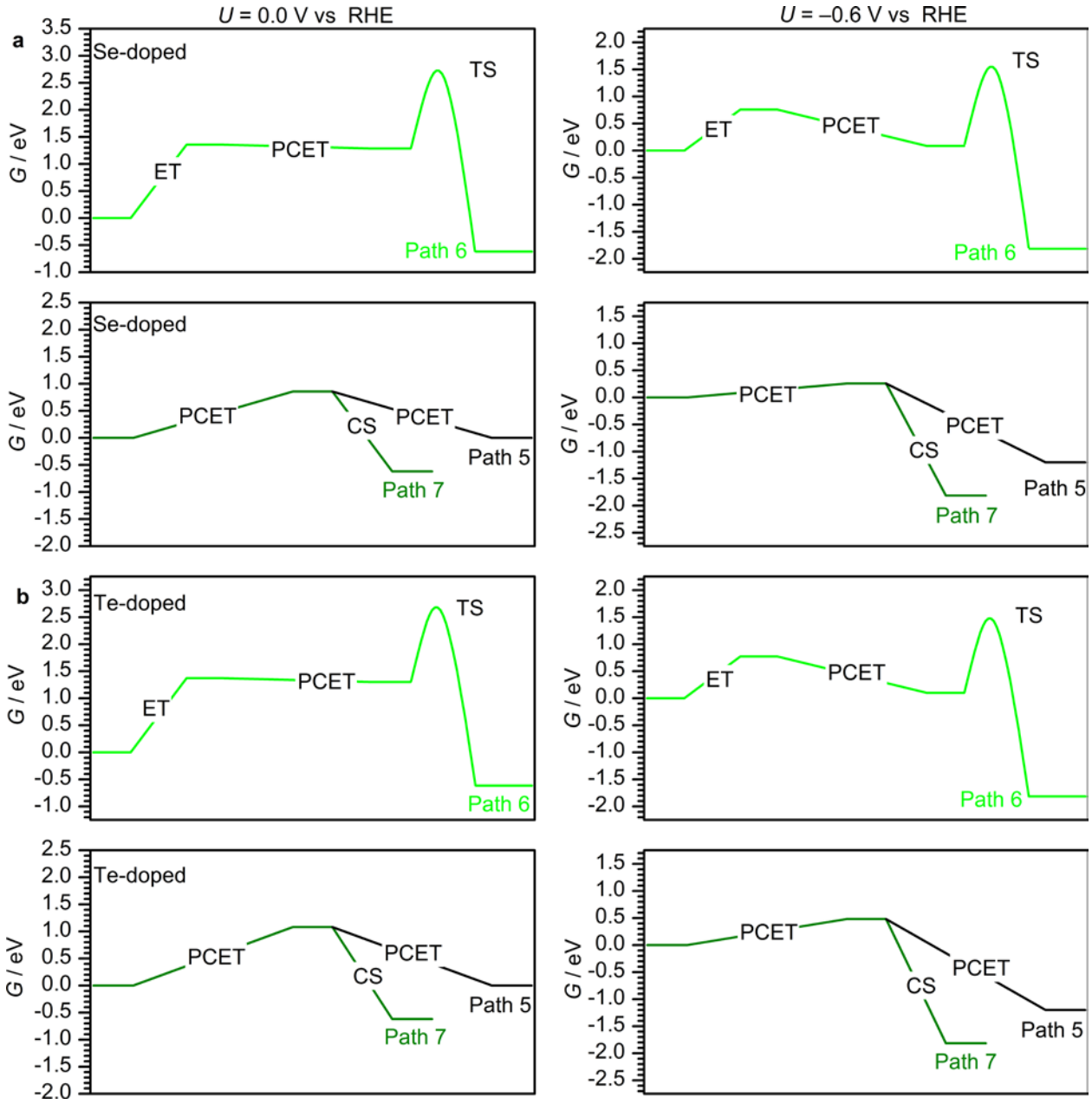

Figure S17. Reaction profiles for CO_2 reduction and hydrogen evolution reactions on (a) selenium-modified Cu(111) surfaces and (b) tellurium-modified Cu(111) surfaces at U = 0.0 and –0.6 V vs RHE. The colors of the reaction paths are selected according to Scheme 1.

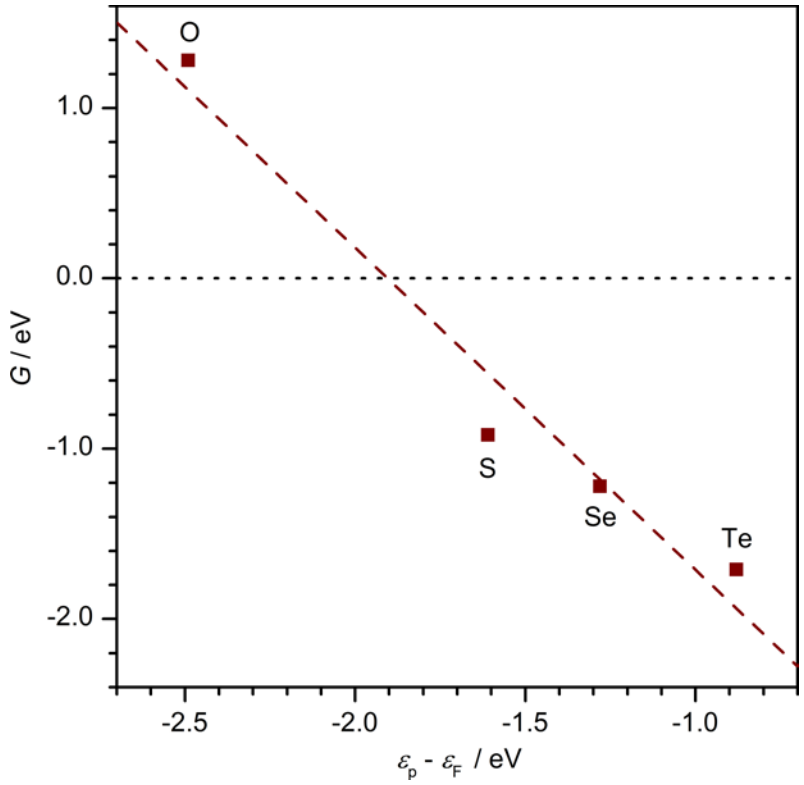

Figure S18. Gibbs free energies of chalcogens adsorbed on Cu(111) as a function of the p-band center of the chalcogen with respect to the Fermi level (X = O, S, Se, Te respectively). $\varepsilon_p - \varepsilon_F$ is a proxy of the basicity.[24]

5. Supplementary Tables

Table S1. Core-level shifts in the Cu 2p region of the copper-chalcogen models simulated by DFT, $\Delta E_{\mathrm{Cu,2p}}$, in eV. The shifts were done with respect to Cu atoms in the bulk metal.

system	$\Delta BE_{\mathrm{Cu,2p}}$
Cu(111)-O	–0.36
Cu(111)-S	–0.03
Cu(111)-Se	< 0.01
Cu(111)-Te	+0.08
Cu_2O(111)	+0.33
Cu_2S(001)	+0.25
Cu_2Se(111)	+1.16
Cu_2Te(001)	+0.59

Table S2. Stability of the chalcogen decorations on Cu(111). Chalcogen: X = O, S, Se, Te. $G_{X,\mathrm{ads}}$: adsorption of X as an adatom on Cu, in eV. $G_{X,\mathrm{sub}}$: substitution energy of a surface Cu by a chalcogen X with respect to H_2X, in eV, in good agreement with ref 25. $G_{X,ki}$: absorption of X at tetrahedral (k=t) or octahedral (k=o) sites of the first (i=1) and second (i=2) interstitial layers, in eV.

X	$G_{X,\mathrm{ads}}$	$G_{X,\mathrm{sub}}$	$G_{X,\mathrm{t1}}$	$G_{X,\mathrm{t2}}$	$G_{X,\mathrm{o1}}$	$G_{X,\mathrm{o2}}$
O	+1.28	+5.86[a]	+3.36	+3.55	+2.84	+3.01
S	–0.92	+2.87	n.c.	+2.98	+1.90	+2.55
Se	–1.22	+2.26	n.c.	+2.90	+1.87	+3.15
Te	–1.71	+1.38	n.c.	+2.55	+1.40	+3.16

n.c.: not converged.

[a] For $G_{\mathrm{O,sub}}$ the corresponding value with respect to O_2 is +3.15 eV.

Table S3. Properties of the chalcogen-decorated Cu surfaces. ΔG_{H_2X}, ΔG_{HX^-} and $\Delta G_{XCO_2H_2}$: desorption energies of the chalcogens, in eV, to produce H_2X, HX^-, and XCO_2H_2, X = O, S, Se, Te. q_{X*} : Bader charges of the adsorbed chalcogens, in $|e^-|$. $\varepsilon_p - \varepsilon_F$: center of the chalcogen' p-band with respect to the Fermi level of the system, in eV. $\Delta(\varepsilon_d - \varepsilon_F)$: shift in the d-band center for the Cu atoms upon anchoring of the chalcogen with respect to the Fermi level, in eV.

system	ΔG_{H_2X}	ΔG_{HX^-}	$\Delta G_{XCO_2H_2}$	q_{X*}	$\varepsilon_p - \varepsilon_F$	$\Delta(\varepsilon_d - \varepsilon_F)$
Cu(111)-O	–1.28	–0.84	+1.86	–0.93	–2.50	–0.16
Cu(211)-O	–1.13	–0.69	+0.24	–0.99	–3.02	–0.02
Cu(110)-O	–1.36	–0.91	+0.40	–1.02	–2.13	–0.01
Cu(100)-O	–0.67	–0.23	+0.81	–1.01	–2.93	–0.01
Cu(111)-OH	–0.60	–0.16	–	–0.59	–4.22	–0.11
Cu(211)-OH	–0.21	+0.23	–	–0.54	–4.21	–0.03
Cu(110)-OH	–0.93	–0.49	–	–0.63	–3.09	–0.03
Cu(100)-OH	–0.27	+0.17	–	–0.60	–4.82	0.00
Cu(111)-S	+0.92	+0.94	+2.95	–0.59	–1.61	–0.07
Cu(211)-S	+1.36	+1.38	+0.95	–0.68	–2.62	–0.04
Cu(110)-S	+1.32	+1.34	+0.84	–0.75	–1.59	–0.07
Cu(100)-S	+1.69	+1.71	+2.03	–0.67	–2.24	0.00
Cu(111)-Se	+1.22	+1.06	+3.74	–0.43	–1.28	–0.05
Cu(211)-Se	+1.71	+1.55	+1.37	–0.49	–2.27	–0.04
Cu(110)-Se	+1.68	+1.53	+1.27	–0.52	–1.22	–0.06
Cu(100)-Se	+1.94	+1.79	+2.29	–0.49	–1.86	–0.01
Cu(111)-Te	+1.71	+1.48	+0.87	–0.21	–0.88	–0.07
Cu(211)-Te	+2.28	+2.05	+2.00	–0.23	–1.85	–0.05
Cu(110)-Te	+2.26	+2.03	+1.88	–0.26	–0.80	–0.07
Cu(100)-Te	+2.36	+2.13	+2.88	–0.24	–1.41	–0.02

Table S4. Adsorption energies of *CO_2 and H* on Cu and atop a *X* atom, *X* = O, S, Se, Te. $\Delta G_{\mathrm{ads,CO_2^*}}$ and $\Delta G_{\mathrm{ads,H^*}}$: adsorption energies for CO_2 and H* on Cu with respect to CO_2 (g) and H_2 (g), in eV. $\Delta G_{\mathrm{ads},X\mathrm{CO_2^*}}$ and $\Delta G_{\mathrm{ads},X\mathrm{H^*}}$: adsorption energies for CO_2 and H* atop an adsorbed *X*, in eV. $\alpha_{\mathrm{ads,CO_2^*}}$ and $\alpha_{\mathrm{ads},X\mathrm{CO_2^*}}$: CO_2 activation angle after adsorption, in degrees.

system	$\Delta G_{\mathrm{ads,CO_2^*}}$	$\alpha_{\mathrm{ads,CO_2^*}}$	$\Delta G_{\mathrm{ads,H^*}}$	$\Delta G_{\mathrm{ads},X\mathrm{CO_2^*}}$	$\alpha_{\mathrm{ads},X\mathrm{CO_2^*}}$	$\Delta G_{\mathrm{ads},X\mathrm{H^*}}$
Cu(111)	+0.73	119	–0.14	–	–	–
Cu(211)	+1.24	119	–0.03	–	–	–
Cu(110)	+0.96	120	–0.06	–	–	–
Cu(100)	+0.71	119	–0.12	–	–	–
Cu(111)–O	+1.17	118	–0.09	+0.55	117	–0.68
Cu(211)–O	+0.86	117	–0.16	+0.26	117	–0.92
Cu(110)–O	+0.63	116	–0.06	–0.13	115	–0.42
Cu(100)–O	+0.89	120	–0.15	+0.84	122	–0.40
Cu(111)–S	+1.26	118	–0.07	+1.47	119	+0.57
Cu(211)–S	+0.88	116	–0.04	+1.67	126	+0.75
Cu(110)–S	+0.99	117	–0.08	+1.83	124	+0.84
Cu(100)–S	+0.90	120	–0.17	+1.59	125	+0.70
Cu_2S(001)	–	–	–	+1.16	120	–0.12
Cu(111)–Se	+1.19	118	–0.07	+1.57	119	+0.93
Cu(211)–Se	+0.87	115	–0.12	+1.71	127	+0.72
Cu(110)–Se	+0.94	117	–0.08	+1.89	125	+1.09
Cu(100)–Se	+0.92	120	–0.18	+1.72	126	+1.03
Cu(111)–Te	+1.17	118	–0.07	+1.59	119	+1.15
Cu(211)–Te	+0.90	114	–0.13	+1.79	127	+1.20
Cu(110)–Te	+0.95	117	–0.09	+1.97	124	+1.28
Cu(100)–Te	+0.91	120	–0.19	+1.68	126	+1.20

6. References

(1) Shinagawa, T.; Larrazábal, G. O.; Martín, A. J.; Krumeich, F.; Pérez-Ramírez, J. Sulfur-Modified Copper Catalysts for the Electrochemical Reduction of Carbon Dioxide to Formate. *ACS Catal.* **2018**, *8*, 837–844.

(2) Larrazábal, G. O.; Martín, A. J.; Krumeich, F.; Hauert, R.; Pérez-Ramírez, J. Solvothermally-Prepared Cu_2O Electrocatalysts for CO_2 Reduction with Tunable Selectivity by the Introduction of p-Block Elements. *ChemSusChem* **2017**, *10*, 1255–1265.

(3) Kresse, G.; Furthmüller, J. Efficiency of Ab-Initio Total Energy Calculations for Metals and Semiconductors Using a Plane-Wave Basis Set. *Comput. Mater. Sci.* **1996**, *6*, 15–50.

(4) Kresse, G.; Furthmüller, J. Efficient Iterative Schemes for Ab Initio Total-Energy Calculations Using a Plane-Wave Basis Set. *Phys. Rev. B* **1996**, *54*, 11169–11186.

(5) Perdew, J. P.; Burke, K.; Ernzerhof, M. Generalized Gradient Approximation Made Simple. *Phys. Rev. Lett.* **1996**, *77*, 3865–3868.

(6) Grimme, S. Semiempirical GGA-Type Density Functional Constructed with a Long-Range Dispersion Correction. *J. Comput. Chem.* **2006**, *27*, 1787–1799.

(7) Bučko, T.; Hafner, J.; Lebègue, S.; Ángyán, J. G. Improved Description of the Structure of Molecular and Layered Crystals: Ab Initio DFT Calculations with van Der Waals Corrections. *J. Phys. Chem. A* **2010**, *114*, 11814–11824.

(8) Almora-Barrios, N.; Carchini, G.; Błoński, P.; López, N. Costless Derivation of Dispersion Coefficients for Metal Surfaces. *J. Chem. Theory Comput.* **2014**, *10*, 5002–5009.

(9) Garcia-Ratés, M.; López, N. Multigrid-Based Methodology for Implicit Solvation Models in Periodic DFT. *J. Chem. Theory Comput.* **2016**, *12*, 1331–1341.

(10) Garcia-Ratés, M.; García-Muelas, R.; López, N. Solvation Effects on Methanol Decomposition on Pd(111), Pt(111), and Ru(0001). *J. Phys. Chem. C* **2017**, *121*, 13803–13809.

(11) Blöchl, P. E. Projector Augmented-Wave Method. *Phys. Rev. B* **1994**, *50*, 17953–17979.

(12) Kresse, G.; Joubert, D. From Ultrasoft Pseudopotentials to the Projector Augmented-Wave Method. *Phys. Rev. B* **1999**, *59*, 1758–1775.

(13) Monkhorst, H. J.; Pack, J. D. Special Points for Brillouin-Zone Integrations. *Phys. Rev. B* **1976**, *13*, 5188–5192.

(14) Makov, G.; Payne, M. Periodic Boundary Conditions in Ab Initio Calculations. *Phys. Rev. B* **1995**, *51*, 4014–4022.

(15) Peterson, A. A.; Abild-Pedersen, F.; Studt, F.; Rossmeisl, J.; Nørskov, J. K. How Copper Catalyzes the Electroreduction of Carbon Dioxide into Hydrocarbon Fuels. *Energy Environ. Sci.* **2010**, *3*, 1311–1315.

(16) Nørskov, J. K.; Rossmeisl, J.; Logadottir, A.; Lindqvist, L.; Kitchin, J. R.; Bligaard, T.; Jónsson, H. Origin of the Overpotential for Oxygen Reduction at a Fuel-Cell Cathode. *J. Phys. Chem. B* **2004**, *108*, 17886–17892.

(17) Murata, A.; Hori, Y. Product Selectivity Affected by Cationic Species in Electrochemical Reduction of CO_2 and CO at a Cu Electrode. *Bull. Chem. Soc. Jpn.* **1991**, *64*, 123–127.

(18) Singh, M. R.; Kwon, Y.; Lum, Y.; Ager, J. W.; Bell, A. T. Hydrolysis of Electrolyte Cations Enhances the Electrochemical Reduction of CO_2 over Ag and Cu. *J. Am. Chem. Soc.* **2016**, *138*, 13006–13012.

(19) Resasco, J.; Chen, L. D.; Clark, E.; Tsai, C.; Hahn, C.; Jaramillo, T. F.; Chan, K.; Bell, A. T. Promoter Effects of Alkali Metal Cations on the Electrochemical Reduction of Carbon

Dioxide. *J. Am. Chem. Soc.* **2017**, *139*, 11277–11287.

(20) The National Institute for Standards and Technology (NIST). X-ray Photoelectron Spectroscopy Database. DOI: 10.18434/T4T88K.

(21) Puigdomenech, I. HydraMedusa. www.kth.se/che/medusa.

(22) Ma, R.; Stegemeier, J.; Levard, C.; Dale, J. G.; Noack, C. W.; Yang, T.; Brown, G. E. J.; Lowry, G. V. Sulfidation of Copper Oxide Nanoparticles and Properties of Resulting Copper Sulfide. *Environ. Sci. Nano* **2014**, *1*, 347–357.

(23) Huang, H.-H. The Eh-pH Diagram and Its Advances. *Metals* **2016**, *6*, 1–30.

(24) Torres, D.; López, N.; Illas, F.; Lambert, R. M. Low-Basicity Oxygen Atoms: A Key in the Search for Propylene Epoxidation Catalysts. *Angew. Chem., Int. Ed.* **2007**, *46*, 2055–2058.

(25) Deng, Y.; Huang, Y.; Ren, D.; Handoko, A. D.; Seh, Z. W.; Hirunsit, P.; Yeo, B. S. On the Role of Sulfur for the Selective Electrochemical Reduction of CO_2 to Formate on CuS_x Catalysts. *ACS Appl. Mater. Interfaces* **2018**, *10*, 28572–28581.